Mid-wave Infrared sensitized InGaAs using Intraband Transition in Doped Colloidal II-VI Nanocrystals

Adrien Khalili, Mariarosa Cavallo, Tung Huu Dang, Corentin Dabard, Huichen Zhang, Erwan Bossavit, Claire Abadie, Yoann Prado, Xiang Zhen Xu, Sandrine Ithurria, et al.

Mid-wave Infrared sensitized InGaAs using Intraband Transition in Doped Colloidal II-VI Nanocrystals

Adrien Khalili[1], Mariarosa Cavallo[1], Tung Huu Dang[1], Corentin Dabard[1], Huichen Zhang[1], Erwan Bossavit[1], Claire Abadie[1], Yoann Prado[1], Xiang Zhen Xu[2], Sandrine Ithurria[2], Grégory Vincent[3], Christophe Coinon[4], Ludovic Desplanque[4], Emmanuel Lhuillier[1*]

[1]Sorbonne Université, CNRS - UMR 7588, Institut des NanoSciences de Paris, INSP, F-75005 Paris, France.
[2] Laboratoire de Physique et d'Etude des Matériaux, ESPCI-Paris, PSL Research University, Sorbonne Université Univ Paris 06, CNRS UMR 8213, 10 rue Vauquelin 75005 Paris, France.
[3]ONERA - The French Aerospace Lab, 6, chemin de la Vauve aux Granges, BP 80100, 91123 Palaiseau, France.
[4]Univ. Lille, CNRS, Centrale Lille, Univ. Polytechnique Hauts-de-France, Junia, UMR 8520 - IEMN, F-59000 Lille, France

Abstract: Narrow bandgap nanocrystals (NCs) are now used as infrared light absorbers, making them competitors to epitaxially grown semiconductors. However, these two types of material could benefit from one another. While bulk materials are more effective in transporting carriers and give a high degree of doping tunability, nanocrystals offer a larger spectral tunability without lattice-matching constraint. Here, we investigate the potential of sensitizing InGaAs in the mid-wave infrared throughout the intraband transition of self-doped HgSe NCs. Our device geometry enables the design of a photodiode remaining mostly unreported for intraband-absorbing NCs. Finally, this strategy allows for more effective cooling and preserves detectivity above 10^8 Jones up to 200 K, making it closer to cryo-free operation for mid-infrared NC-based sensors.

Keywords: InGaAs, HgSe, nanowire, quantum dot, mid-wave infrared, light sensing, photodiode

*To whom correspondence should be sent: el@insp.upmc.fr

INTRODUCTION

Infrared (IR) sensing in the short- (up to 2 µm) and mid-wave infrared (3-5 µm range) is driven by narrow band gap semiconductors grown under thin film form.[1] In order to build a high-quality film, the semiconductor layer must be lattice matched. This prevents its spectral tunability as the latter results from alloying, which induces a change in the lattice parameter.[2] The use of Van der Waals heterostructures[3] can, however, overcome this lattice matching constraint. This approach was initially developed for 2D materials and has only lately been extended to mixed material dimensionality.[4] Light sensitization of graphene by colloidal nanocrystals[5–7] (NCs), in particular, has led to devices with high photoresponsivity. This strategy is nonetheless not limited to 2D materials and NCs and can be applied to any dimensionality,[8] including bulk materials.[9,10] Because colloidal NCs lift the constraint of epitaxial growth, it is relevant to use them to broaden the spectral response of bulk materials absorbing only in the near IR range.

Moreover, coupling bulk semiconductors with NCs can be valuable to overcome the limited control over doping in colloidal particles. IR absorbing IV-VI[11,12] and II-VI[13] semiconductor NCs mostly present an *n*-type nature cannot be degenerately doped under *p*-type form.[14] Consequently, it is of utmost interest to consider the NC/bulk heterostructure as a path to design a NC-based *pn* junction, which is otherwise challenging unless[14] a ligand exchange is conducted to enable an ambipolar operation of the material.

Here, we explore the design of a mid-wave infrared (MWIR) photodiode combining an array of InGaAs nanowires as hole transporting material together with HgSe NCs as MWIR absorbers. Compared to the previous work by Khalili *et al*,[10] where the authors coupled *n*-type InGaAs nanowires to *p*-type short-wave infrared (SWIR) HgTe NCs, this work aims to expand the spectral sensitization of bulk semiconductors toward longer wavelengths (5 µm cut off targeted). This raises clear challenges since the interfacial barrier for the charge transfer also increases.

To achieve MWIR operations, we intend to use the intraband transition in self-doped HgSe NCs,[15,16] see **Figure 1**d. However, an array of such intraband particles tends to have a weak and slow photoresponse together with a high dark current and a low thermal activation (i.e., cooling barely reduces the dark current), significantly limiting its potential for IR sensing.[14,17–19] Several strategies have been proposed to address these limitations, including careful control of the carrier density[14,17] and growth of core-shell NCs.[18] Here, we focus on the approach proposed by Livache *et al.*, where HgSe NCs are blended with quasi-intrinsic HgTe NCs to achieve a metamaterial combining MWIR absorption with low dark current and fast response. This *n*-type blend is then coupled with *p*-type InGaAs nanowires, which extract the holes and form a photodiode.

METHODS

Chemicals*:* Mercury chloride ($HgCl_2$, Sigma-Aldrich, 99%), mercury acetate ($Hg(OAc)_2$**,** Alfa Aesar, >98%), **Mercury compounds are highly toxic. Handle them with special care.** tellurium powder (Te, Sigma-Aldrich, 99.99%), selenium powder (Se, Alfa Aesar, >99%), trioctylphosphine (TOP, Alfa Aesar, 90%), oleylamine (OLA, Acros, 80-90%), dodecanethiol (DDT, Sigma-Aldrich, 98%), acetone (VWR), isopropanol (IPA, VWR), ethanol absolute anhydrous (EtOH, VWR), methanol (VWR, >98%), hexane (VWR, 99%), 2-mercaptoethanol (MPOH, Merck, >99%), N,N dimethylformamide (DMF, VWR), toluene (VWR, 99.8%), methylisobutylketone (MIBK, VWR, >98.5%), ammonia (NH_3, 30%, Carlo Erba Reagents). All chemicals are used without further purification except oleylamine that is centrifuged before use.

1 M TOP:Te*:* 2.54 g of Te powder are mixed in 20 mL of TOP in a three neck flask. The flask is kept under vacuum at room temperature for 5 min and then the temperature is raised to 100 °C.

Furthermore, degassing of flask is conducted for the next 20 min. The atmosphere is switched to nitrogen and the temperature is raised to 275 °C. The solution is stirred until a clear orange coloration is obtained. The flask is cooled down to room temperature and the color change to yellow. Finally, this solution is transferred to a nitrogen filled glove box for storage.

1 M TOP:Se precursor: 1.54 g of Se powder is sonicated in 20 mL of TOP until a colorless solution is obtained

HgSe 2.2k: In a 50 mL three neck flask, 500 mg of $Hg(OAc)_2$, 10 mL of oleic acid and 25 mL of oleylamine are degassed under vacuum at 85 °C. Meanwhile, 1.6 mL of TOP:Se (1 M) are extracted from the glove box. After the atmosphere is switched to N_2 and the temperature stabilized at 100 °C, the TOP:Se solution is quickly injected. After 3 min, 1 mL of DDT (6.6 mmol) is injected and a water bath is used to quickly decrease the temperature. The content of the flask is split over 2 centrifuge tubes and EtOH is added. After centrifugation, the formed pellets are redispersed in one centrifuge tube with toluene and one drop of DDT. The solution is precipitated a second time using ethanol. Again, the formed pellet is redispersed in toluene and one drop of DDT. At this step the CQDs are centrifuged in pure toluene to get rid of the lamellar phases. The solid phase is discarded. The stable phase is transferred in a weighted tube and finally precipitated using methanol. The solid is dried under vacuum for 30 min (in glove box vacuum chamber). Finally, CQDs are redispersed with a 50 $mg.mL^{-1}$ concentration in toluene.

HgTe 4k: In a 100 mL three neck flask, 543 mg of $HgCl_2$ and 50 mL of oleylamine are degassed under vacuum at 110 °C. Meanwhile, 2 mL of TOP:Te (1 M) are extracted from the glove box and mixed with 8 mL of oleylamine. After the atmosphere is switched to N_2 and the temperature stabilized at 80 °C, the TOP:Te solution is quickly injected. After 3 min, 10 mL of a mixture of DDT in toluene (10% of DDT) is injected and a water bath is used to quickly decrease the temperature. The content of the flask is split over 4 centrifuge tubes and MeOH is added. After centrifugation, the formed pellets are redispersed in one centrifuge tube with toluene. The solution is precipitated a second time using ethanol. Again, the formed pellet is redispersed in toluene. At this step the CQDs are centrifuged in pure toluene to get rid of the lamellar phases. The solid phase is discarded. The stable phase is transferred in a weighted tube and finally precipitated using methanol. The solid is dried under vacuum for 30 min (in glove box vacuum chamber). Finally, CQDs are redispersed with a 50 $mg.mL^{-1}$ concentration in toluene.

HgSe:HgTe mixture preparation: Two solutions of HgSe and HgTe are mixed in order to obtain an absorbance ratio of 1:1. A drop of the mixture is dried on the diamond cell of a Fisher IS50 Fourier transform infrared spectrometer. In ATR configuration, between 8 000 and 400 cm^{-1} we acquire a spectrum of the mixture. Transmission electron microscopy of the mixture confirms the presence of the two materials. Their very different shape makes that they can be distinguished from the regular imaging, where HgSe appears as quasi sphere and where HgTe appears as branched particles, see Figure 1 and S1.

HgTe/HgSe ink*:* 1.5 mL of the mixture NC solution in toluene is mixed with 2.5 mL of exchange solution (15 mg $HgCl_2$ + 1 mL MPOH + 9 mL DMF) and 2.5 mL of DMF to induce a phase transfer toward the polar phase. 5 mL of hexane is added to the solution and mixed with vortex and sonication. After a few seconds, two phases are clearly visible and the hexane phase is removed. The solution is cleaned with hexane one more time. Then, the solution is precipitated by adding toluene and centrifuged at 6000 rpm for 3 min. The pellet is dried under vacuum. Supernatant is discarded and the NCs are redispersed in 300 µL of DMF. Finally, the ink is filtered through a 0.22 µm PTFE filter.

Transmission electron microscopy: For TEM imaging, a drop of diluted NCs solution is casted on a copper grid covered with an amorphous carbon film. The grid is degassed overnight under secondary vacuum. A JEOL 2010F is used at 200 kV for the acquisition of pictures.

InGaAs nanowires growth: Arrays of in-plane InGaAs *p*-doped nanowires (NWs) are fabricated using atomic hydrogen assisted selective area Molecular Beam Epitaxy (MBE).[20,21] The silicon dioxide mask, prepared by e-beam lithography and reactive ion etching on InP(100) semi-insulating substrate, consists of a 100 µm wide network of 200 [110]-oriented nano-trenches repeated every 500 nm and composed of 20 µm-long and 130 nm wide openings. These arrays are connected in parallel at one end by a larger 5x100 µm opening in the SiO_2 mask. Two other 100 µm long and 130 nm wide trenches are designed crosswise in the middle and at the other end of the NW arrays to anticipate some discontinuity of NWs and ensure electrical conduction. After mask preparation, the sample is introduced in the MBE chamber for InP surface deoxidization under atomic hydrogen and arsenic flux at 500 °C. The subsequent growth consists of the epitaxy of 50 nm InGaAs lattice matched to InP and p-doped with a targeted Beryllium atom density of $5x10^{18}$ cm^{-3}. Atomic hydrogen exposure together with a nominal growth rate of 0.2 $ML.s^{-1}$ ensures a good selectivity for the growth at 490°C.

Fabrication steps: After the growth step, the sample is rinsed with acetone and isopropanol. An adhesion primer (TI-PRIME) is spin-coated onto the substrate and annealed for 2 min at 120 °C before AZ5214E photo-resist is spin-coated and baked at 110 °C for 90s. A MJB4 mask-aligner is used to exposed the sample to UV light for 1.5 s through a lithography mask. Then the sample is baked 2 min at 125 °C to invert the resist and flood-exposed for 40 s. The sample is dipped 30 s in a solution of AZ726 developer before being rinsed in pure water for 15 s. The patterned substrate is dried and cleaned with 5 min of oxygen plasma to remove resist residues. The sample is then dipped few seconds in a solution of NH_3 3% to prevent oxidation of the InGaAs wires. In a thermal evaporator, 5 nm of chromium are deposited as an adhesion promoter before 150 nm of gold are evaporated (**Figure S3d)**. Lift-off is conducted in an acetone bath for at least 1 h. Then, the substrate is rinsed with isopropanol before a layer of A6 PMMA 950 is spin-coated and baked 15 min at 150 °C. The sample is transferred in a Zeiss Supra 40 SEM with Raith ELPHYS Quantum device for electron beam lithography. The operating bias is set to 20 kV and the aperture to 20 µm. The current is measured at 100 pA. The dose is set at 260 $\mu C.cm^{-2}$. The PMMA is developed by dipping the film in a solution of MIBK:isopropanol (1:3) for 50 s and rinsed in pure isopropanol for 20 s. The sample is put under an O_2 plasma to remove residual resists. We dip the sample few seconds in a 3% NH_3 solution to prevent oxidation of the InGaAs wires. We then place the sample in an Alcatel sputtering chamber for a 50 min deposition of 100 nm of SiO_x **(Figure S3e)**. The lift-off is performed by dipping the film in acetone overnight. Finally, a solution of the mixture CQDs ink is spin-coated **(Figure S3f)** following a two-step procedure: 1000 rpm for 120 s followed by 3000 rpm for 60 s. The final thickness is in the 200-400 nm range.

Electromagnetic simulation: The complex optical index for InP,[22] InGaAs,[22] HgTe[23] and HgSe[24] are taken from literature cited. We assume that n_{SiO2} = 1.45 and k_{SiO2} = 0. Maps of the electromagnetic power loss density have been calculated with RF Toolbox from COMSOL commercial software based on the Finite Elements Method (FEM) under transverse magnetic or transverse electric polarization (magnetic or electric field parallel with the wires, respectively). Floquet periodicity is chosen as boundary conditions in the plane direction. Ports are implemented at the top and bottom limits and diffracted orders are considered. Mesh has a triangular pattern. The period of the grating is 700 nm. Thickness of the nanowires is 50 nm, their bottom and top widths

are 130 nm and 70 nm, respectively. The thicknesses of the silica and NCs layers are 15 nm and 300 nm, respectively. The thickness of the InP substrate has no influence on the absorption of NCs, InGaAs or SiO_2.

FTIR spectra: FTIR spectra are acquired using a Fisher IS50 Fourier transform infrared spectrometer. To measure CQD absorption, we use the spectrometer in ATR configuration. A drop of CQD solution is dried on the diamond cell. The source is an infrared light, and the detector is a DTGS ATR. Spectra are typically acquired between 8 000 and 400 cm^{-1} with a 4 cm^{-1} resolution and averaged over 32 spectra.

Activation energy measurements: Devices are mounted on the cold finger of a closed-cycle cryostat equipped with cold shield. The samples are cooled down to 80 K, and current flow is measured with a Keithley 2634b source-meter which also applies bias to the sample. Temperature is measured with a Lakeshore 325 temperature controller using a calibrated sensor on the sample holder. Resulting $I(T)$ curves are fitted to an Arrhenius model ($I_0 = Ae^{-E_a/kT}$) between 300 K and 80K, allowing for the extraction of the activation energy E_a.

DC transport measurements: The sample is connected to a dual channel Keithley 2634b, which controls the drain bias (V_{DS}) and measures the associated current (I_{DS}). This measure is carried out in the dark or under illumination using a 4.42 µm QCL

Photocurrent spectra: The device is enclosed in a closed-cycle cryostat and cooled down to the desired temperature. The head of the cryostat is brought in the sample compartment of a Fischer iS50 FTIR spectrometer and illumination is provided by the focused Globar source through two ZnSe windows (one on the outer cryostat enclosure and one on the cold shield). The photocurrent is amplified using a Femto DLPCA−200 transimpedance amplifier, which also serves as a bias source. Output of the amplifier is sent back to the FTIR spectrometer through the ad hoc external detector adapter. All spectra are normalized to the background spectrum, acquired with a flat-response DTGS detector in the same spectral range to account for source and optical path spectra.

Responsivity measurement: The source is a blackbody at 980 °C placed 30 cm away from the sample. A germanium filter is utilized to suppress the high energy part of the blackbody spectrum. The total power calculated according to the formula: $P = A_D.\pi.cos(\beta).sin^2(\alpha).\int_{\lambda_{min}}^{\lambda_{max}} \frac{hc^2}{\lambda^5}.\frac{1}{e^{hc/\lambda kT}}d\lambda$ where α is the solid angle illuminated, β is the angle of the sample (0° corresponds to sample perpendicular to the light illumination), A_D is the device area, h is the Planck constant, c the light velocity, k is the Boltzmann constant and T the temperature. The light is chopped from 1 Hz to 100 Hz. The photocurrent is measured using Zurich Instruments MFLI lock-in amplifier. The sample is mounted on the cold finger of a close cycle cryostat.

Noise measurement. Current from the device (at -10 V bias, kept in the dark) is amplified by a Femto DLPCA-200, then fed into a SRS SR780 spectrum analyzer. The sample is mounted on the cold finger of a close cycle cryostat.

Detectivity determination. The specific detectivity (in Jones) of the sample is determined using the formula: $D^* = \frac{R\sqrt{A}}{S_I}$, where R (in $A.W^{-1}$) is the responsivity, S_I is the noise ($A/\sqrt{Hz}$) and A the area of the device (cm^2).

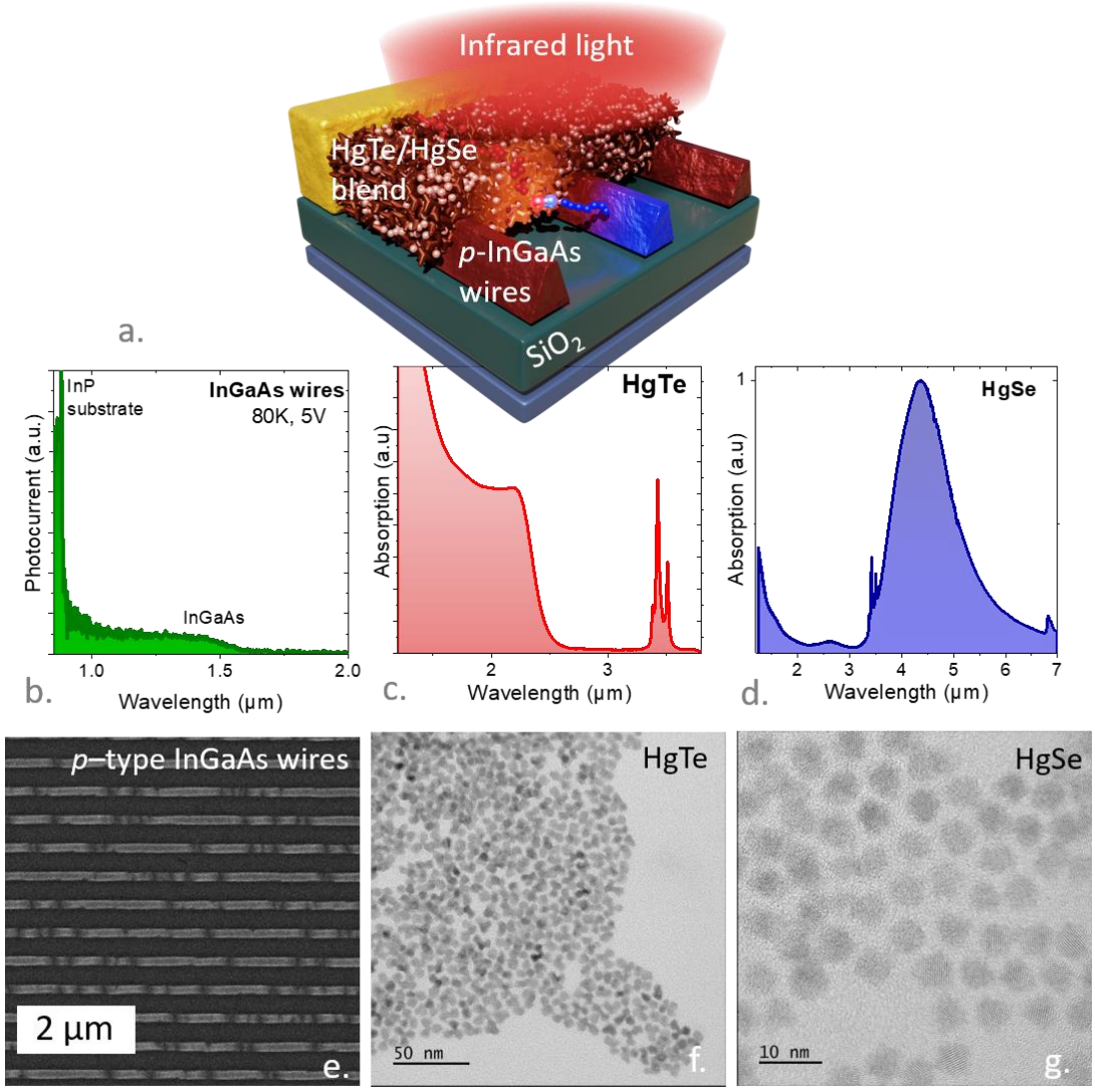

Figure 1 Mid-wave infrared absorbing material properties. *a. Schematic of the device with the InGaAs nanowires coated with the HgSe/HgTe mixture. b. Photocurrent spectrum of the InGaAs nanowires at 80K under 5 V bias. c. and d. are absorption spectra of HgTe NCs and HgSe NCs respectively. e. SEM image of the InGaAs nanowires. f. and g. are TEM images of HgTe NCs and HgSe NCs respectively.*

RESULTS AND DISCUSSION

The targeted structure is depicted in **Figure 1**a, and the main fabrication steps are described in Figure S3. The InGaAs wires are first grown using a selective epitaxy procedure. To do so, an InP substrate is coated with silica, and openings are etched, allowing InGaAs growth using molecular beam epitaxy. Here we functionalized the substrate to form an array of parallel nanowires that are 100 µm long, 130 nm wide, and 50 nm thick, see **Figure 1**e. The dimension of the wire being large, no quantum confinement is expected. The nanowires are then connected to one electrode, but remain isolated from the second one, see Figure S4. The electrode in contact with the wire array is then buried under a silica layer to ensure that the charge conduction occurs via the nanowires. HgTe[25] and HgSe[26] NCs are grown using conventional colloidal growth procedures. HgTe presents a branched aspect[27] as revealed by transmission electron microscopy (TEM), see **Figure 1**f. The absorption spectrum presents an edge of around 2.5 µm. At longer wavelengths, a narrow doublet from the C-H resonance is observed and is attributed to the capping ligands (dodecanethiol after synthesis) that contain alkyl chains. For HgSe, the particle shape is closer to a sphere, and the

absorption spectrum is dominated by the intraband transition ranging from 3 to 5 µm. These particles are then blended (the benefit of the blend is better described in Figure S1 and S2) with a previously optimized ratio corresponding roughly to a 1:1 particle ratio. This ratio was determined empirically such that the amount of HgTe is sufficient to prevent the transport percolation within HgSe NCs,[19] see Figure S2. Finally, this blend is transformed into a photoconductive ink by replacing the initial long and insulating ligands by shorter ones[28,29] ($HgCl_2$ ions and mercaptoethanol).
Spectrally, neither InGaAs (≈1.5 µm cut-off at 80 K see **Figure 1**b) nor HgTe present absorption within the MWIR, leaving HgSe as the sole MWIR sensitizer material. Simulations of the absorption spectra of the different materials in the device are given in **Figure 2**a. The absorption spectrum of the complete device is clearly dominated by the NC absorption (*i.e.,* over the III-V layer and its substrate), with a small bump between HgTe and HgSe signals due to the OH absorption from the mercaptoethanol ligands used to make the blend conductive. The absorption maps, see **Figure 2**b-d, confirm that the III-V layers do not absorb above 2 µm.

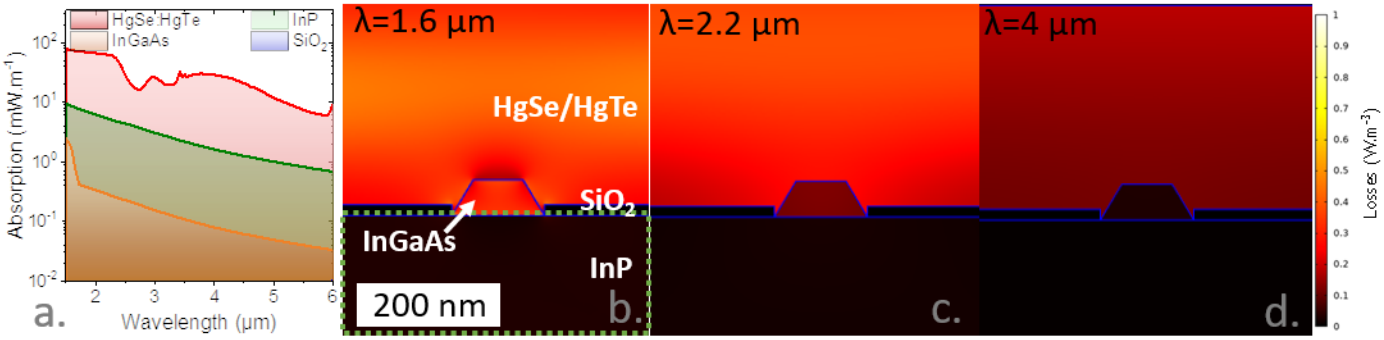

Figure 2 Spectroscopic properties of the photocurrent. *a. Simulated absorption spectra of the hybrid structure under TM polarization withing the different materials of the structure. b. c. and d. are simulated absorption maps under TM polarization at 1.6 µm (below InGaAs bandgap), 2.2 µm (above InGaAs bandgap) and 4 µm (at the intraband), respectively.*

Electrically, the device behaves as a diode with a strongly rectifying IV curve, see **Figure 3**a, which highlights the benefit of the III-V wires compared to a device with gold electrodes. In this system, the InGaAs nanowires with its p-doped nature act as an unipolar barrier by blocking the electrons (see Figure S8). A rectifying behavior still remains present even at room temperature, whereas most NC-based MWIR diodes tend to lose this rectification for operation away from cryogenic temperatures.[30] Furthermore, the transport is strongly dependent on the temperature, making the sample cooling a viable strategy to reduce the dark current as opposed to a pristine array of degenerately doped NCs.[12,18,19,24,31] The extracted activation energy is 163 meV (Figure S9), which corresponds to half of the intraband gap energy. This is the highest value reported for transport in intraband particles at this wavelength, highlighting the benefit of our geometry.

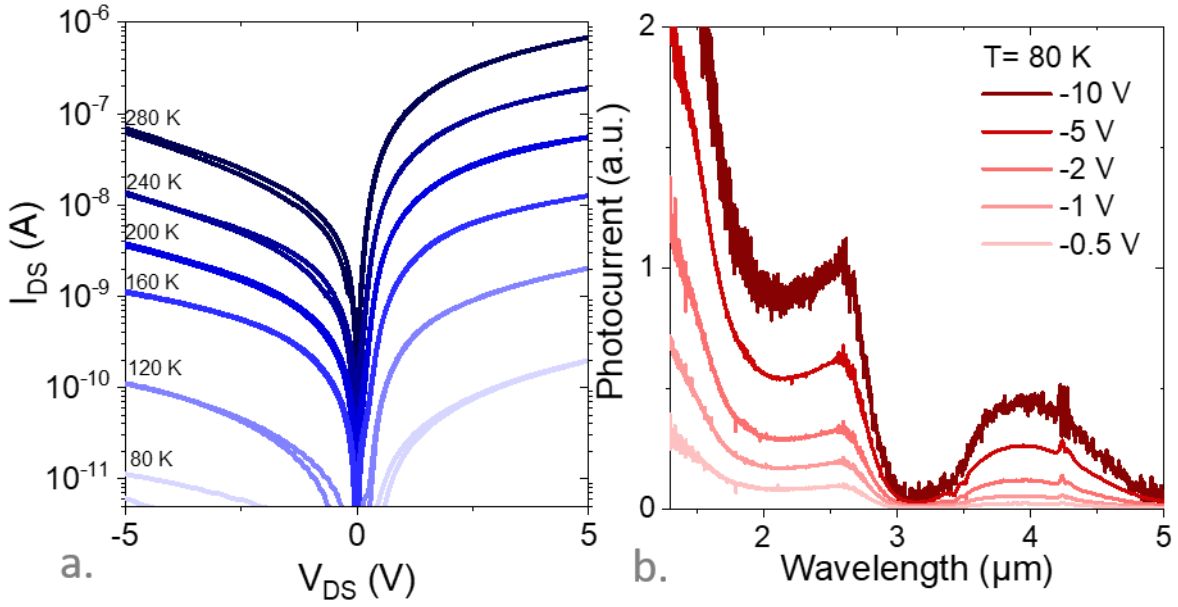

Figure 3 Transport properties of the intraband hybrid structure. *a. I-V curves under dark conditions, at various temperatures for the heterostructure. b. Photocurrent spectra of the hybrid structure at 80 K under various reversed biases.*

The photocurrent spectra have been acquired under various applied biases, see **Figure 3**b. We can attribute each feature of the spectra to the different materials composing our blend. The signal above 3 µm refers to HgSe intraband absorption, whereas the signal below 3 µm refers to HgTe interband absorption. It is worth pointing out that the OH contribution, present in the absorption, is absent here since ligands are not involved in the photoconductive process. In addition, we also note that the energy splitting between HgTe and HgSe features is reduced compared to the absorption spectra proposed in **Figure 1**. This results from the redshift of interband transition in HgTe[32,33] and blue shift of the intraband in HgSe upon cooling.[26] Finally, below 1.7 µm, we observe a sharp rise of the photocurrent related to the high mobility transport in the InGaAs nanowires[34] ($\mu_{p\text{-}InGaAs} \approx 100$ cm^2.V^{-1}.S^{-1}>>μ_{NC}). Since the geometry promoted conduction across the nanowires, the MWIR photocurrent arises from HgSe absorption leading to a charge transfer to the InGaAs nanowires. Therefore, the MWIR sensitization of the InGaAs can be established.

The responsivity of the device ranges from 6 mA.W^{-1} at room temperature to a decade lower for cryogenic operation (@ 80 K), see **Figure 4**a and S7. We attribute this decrease in the response with temperature to the thermal activation of the mobility inherent to hopping conduction. Certainly, the limited device's responsivity is constrained by a lack of light management strategy[24] leading to an overall weak absorption. Time response under illumination by a quantum cascade laser (λ=4.42 µm) resonant with the intraband absorption is faster than 100 µs, see **Figure 4**b. The noise is limited by a 1/f contribution, as revealed by the inset of **Figure 4**c. The device's detectivity is around 2x10^8 Jones at 80 K, which is one order of magnitude below best intraband devices,[14,19,24], and Table 1 for a comparison of this device with state-of-the-art performances of devices based on the intraband transition in nanocrystal array. However, it preserves this level of performance up to 200 K, whereas the same blend (HgSe/HgTe) presents a detectivity reduced by a factor of 10 when the temperature is increased from 80 K to 160 K.[24] This suggests that the strategy relying on nanowires for charge extraction provides the benefit of a higher operating temperature, reducing the constraint on the device size, weight, and power consumption.

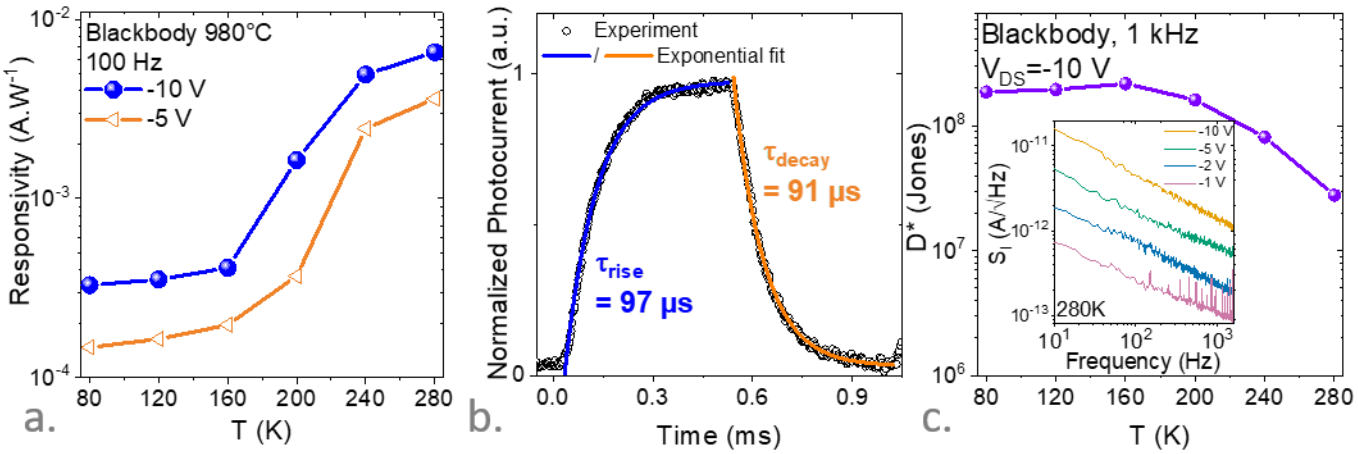

Figure 4 MWIR detection performances from the hybrid structure*. a. Responsivity of the heterostructure as a function of the temperature under -5 V and -10 V with a blackbody illumination. b. Photocurrent response from the hybrid structure to a 1 kHz optically chopped quantum cascade laser (QCL) at 4.42 µm. Data are fitted using exponential decays. c. Specific detectivity under – 10 V as a function of the operating temperature. The inset is the noise current spectral density at 280 K as a function of the signal frequency under various biases.*

Table 1 Figure of merit for nanocrystal-based photodetector based on intraband absorption

Intraband absorbing material	Device structure	λ (µm)	R (mA.W^{-1})	D* (Jones)	Operating T (K)	Times response	Reference
HgSe	Photoconductor	4.4 µm	0.5	8.5x10^8	80 K	-	[35]
HgSe	Photoconductor	6 µm	800	≈ 10^8	300 K	-	[36]
HgSe	Diode	4 µm	5	10^9	80 K	<200 ns	[37]
HgSe	Photoconductor	4.4 µm	3	10^9	80 K	<200 ns	[38]
	+ resonator		2	6x10^7	200 K		
HgSe	Photoconductor	≈4 µm	77	1.7x10^9	80 K	≈µs	[14]
Ag_2Se	Photoconductor	4.8 µm	0.008	-	25 K	seconds	[39]
Ag_2Se	Photoconductor	4.5 µm	0.35	-	90 K	-	[40]
Ag_2Se	Barrier device	4.5 µm	13	3x10^5	300 K	seconds	[41]
Ag_2Se/PbS	Diode	4.5 µm	18	8x10^6	300 K	-	[42]
PbS	Photoconductor	5-9 µm	0.1	~ 10^4	80 K	>200 ms	[12]
HgSe	Diode	4 µm	0.3	2x10^8	80 K	<100 µs	**This work**
			6	2x10^8	200 K		

CONCLUSION

We demonstrate here the coupling of colloidal quantum dots to a bulk semiconductor while lifting the constraint of epitaxial lattice matching. For the first time, this strategy is applied to expand a III-V near-infrared absorber toward the mid-infrared. The benefit is mutual since the hybrid strategy

simplifies the design of a NC-based photodiode in a spectral range where the band alignment remains mostly unknown. Moreover, our strategy also brings the advantage of maintaining a high signal-to-noise ratio up to 200 K, whereas other intraband-based devices can only be operated at cryogenic temperatures. This work paves the way toward mid-wave infrared sensors operating at high temperatures.

SUPPORTING MATERIAL

Supporting material include details about (*i*) benefit of the HgSe/HgTe blend over HgSe for mid IR photoconduction, (*ii*) hybrid structure fabrication and structural characterization and (*iii*) additional optoelectronic characterization of the device.

DATA AVAILABILITY

The data that support the findings of this study are available from the corresponding author upon reasonable request.

ACKNOWLEDEGMENTS

The project is supported by ERC starting grant blackQD (grant n° 756225). We acknowledge the use of clean-room facilities from the “Centrale de Proximité Paris-Centre”. This work has been supported by the Region Ile-de-France in the framework of DIM Nano-K (grant dopQD). This work was supported by French state funds managed by the ANR within the Investissements d'Avenir programme under reference ANR-11-IDEX-0004-02, and more specifically within the framework of the Cluster of Excellence MATISSE and also by the grant IPER-Nano2 (ANR-18CE30-0023-01), Copin (ANR-19-CE24-0022), Frontal (ANR-19-CE09-0017), Graskop (ANR-19-CE09-0026), NITQuantum (ANR-20-ASTR-0008), Bright (ANR-21-CE24-0012), MixDFerro (ANR-21-CE09-0029.) and Quicktera (ANR-22-CE09-0018). This work was partly supported by the French Renatech network.

CONFLICT OF INTEREST

The authors declare no competing interest.

REFERENCES

[1] A. Rogalski, “Narrow-Gap Semiconductors for Infrared Detectors,” in *Handb. Lumin. Semicond. Mater.* (CRC Press, 2012).
[2] D. Benyahia, Ł. Kubiszyn, K. Michalczewski, A. Kębłowski, P. Martyniuk, J. Piotrowski, and A. Rogalski, “Optimization of the interfacial misfit array growth mode of GaSb epilayers on GaAs substrate,” J. Cryst. Growth **483**, 26 (2018).
[3] A. Rogalski, “Van der Waals materials for HOT infrared detectors: A review,” Opto-Electron. Rev. 2022 30 1 E140551 (2022).
[4] D. Jariwala, T.J. Marks, and M.C. Hersam, “Mixed-dimensional van der Waals heterostructures,” Nat. Mater. **16**, 170 (2017).
[5] G. Konstantatos, M. Badioli, L. Gaudreau, J. Osmond, M. Bernechea, F.P.G. de Arquer, F. Gatti, and F.H.L. Koppens, “Hybrid graphene–quantum dot phototransistors with ultrahigh gain,” Nat. Nanotechnol. **7**, 363 (2012).
[6] F.H.L. Koppens, T. Mueller, P. Avouris, A.C. Ferrari, M.S. Vitiello, and M. Polini, “Photodetectors based on graphene, other two-dimensional materials and hybrid systems,” Nat. Nanotechnol. **9**, 780 (2014).

[7] T. Li, X. Tang, and M. Chen, “Room-Temperature Infrared Photodetectors with Zero-Dimensional and New Two-Dimensional Materials,” Coatings **12**, 609 (2022).
[8] H. Jiao, X. Wang, Y. Chen, S. Guo, S. Wu, C. Song, S. Huang, X. Huang, X. Tai, T. Lin, H. Shen, H. Yan, W. Hu, X. Meng, J. Chu, Y. Zhang, and J. Wang, “HgCdTe/black phosphorus van der Waals heterojunction for high-performance polarization-sensitive midwave infrared photodetector,” Sci. Adv. **8**, eabn1811 (2022).
[9] H. Henck, Z. Ben Aziza, O. Zill, D. Pierucci, C.H. Naylor, M.G. Silly, N. Gogneau, F. Oehler, S. Collin, J. Brault, F. Sirotti, F. Bertran, P. Le Fèvre, S. Berciaud, A.T.C. Johnson, E. Lhuillier, J.E. Rault, and A. Ouerghi, “Interface dipole and band bending in the hybrid *p-n* heterojunction MoS_2/GaN(0001),” Phys. Rev. B **96**, 115312 (2017).
[10] A. Khalili, C. Abadie, T.H. Dang, A. Chu, E. Izquierdo, C. Dabard, C. Gréboval, M. Cavallo, H. Zhang, S. Pierini, Y. Prado, X.Z. Xu, S. Ithurria, G. Vincent, C. Coinon, L. Desplanque, and E. Lhuillier, “Colloidal II–VI—Epitaxial III–V heterostructure: A strategy to expand InGaAs spectral response,” Appl. Phys. Lett. **120**, 051101 (2022).
[11] I. Ramiro, B. Kundu, M. Dalmases, O. Özdemir, M. Pedrosa, and G. Konstantatos, “Size- and Temperature-Dependent Intraband Optical Properties of Heavily n-Doped PbS Colloidal Quantum Dot Solid-State Films,” ACS Nano **14**, 7161 (2020).
[12] I. Ramiro, O. Özdemir, S. Christodoulou, S. Gupta, M. Dalmases, I. Torre, and G. Konstantatos, “Mid- and Long-Wave Infrared Optoelectronics via Intraband Transitions in PbS Colloidal Quantum Dots,” Nano Lett. **20**, 1003 (2020).
[13] C. Gréboval, A. Chu, N. Goubet, C. Livache, S. Ithurria, and E. Lhuillier, “Mercury Chalcogenide Quantum Dots: Material Perspective for Device Integration,” Chem. Rev. **121**, 3627 (2021).
[14] M. Chen, Q. Hao, Y. Luo, and X. Tang, “Mid-Infrared Intraband Photodetector via High Carrier Mobility HgSe Colloidal Quantum Dots,” ACS Nano **16**, 11027 (2022).
[15] A. Jagtap, C. Livache, B. Martinez, J. Qu, A. Chu, C. Gréboval, N. Goubet, and E. Lhuillier, “Emergence of intraband transitions in colloidal nanocrystals [Invited],” Opt. Mater. Express **8**, 1174 (2018).
[16] J. Kim, D. Choi, and K. Seob Jeong, “Self-doped colloidal semiconductor nanocrystals with intraband transitions in steady state,” Chem. Commun. **54**, 8435 (2018).
[17] Z. Deng, K.S. Jeong, and P. Guyot-Sionnest, “Colloidal Quantum Dots Intraband Photodetectors,” ACS Nano **8**, 11707 (2014).
[18] N. Goubet, C. Livache, B. Martinez, X.Z. Xu, S. Ithurria, S. Royer, H. Cruguel, G. Patriarche, A. Ouerghi, M. Silly, B. Dubertret, and E. Lhuillier, “Wave-Function Engineering in HgSe/HgTe Colloidal Heterostructures To Enhance Mid-infrared Photoconductive Properties,” Nano Lett. **18**, 4590 (2018).
[19] C. Livache, B. Martinez, N. Goubet, C. Gréboval, J. Qu, A. Chu, S. Royer, S. Ithurria, M.G. Silly, B. Dubertret, and E. Lhuillier, “A colloidal quantum dot infrared photodetector and its use for intraband detection,” Nat. Commun. **10**, 2125 (2019).
[20] A. Bucamp, C. Coinon, J.-L. Codron, D. Troadec, X. Wallart, and L. Desplanque, “Buffer free InGaAs quantum well and in-plane nanostructures on InP grown by atomic hydrogen assisted MBE,” J. Cryst. Growth **512**, 11 (2019).
[21] A. Bucamp, C. Coinon, D. Troadec, S. Lepilliet, G. Patriarche, X. Wallart, and L. Desplanque, “Gate length dependent transport properties of in-plane core-shell nanowires with raised contacts,” Nano Res. **13**, 61 (2020).
[22] S. Adachi, “Optical dispersion relations for GaP, GaAs, GaSb, InP, InAs, InSb, AlxGa1−xAs, and In1−xGaxAsyP1−y,” J. Appl. Phys. **66**, 6030 (1989).
[23] P. Rastogi, A. Chu, T.H. Dang, Y. Prado, C. Gréboval, J. Qu, C. Dabard, A. Khalili, E. Dandeu, B. Fix, X.Z. Xu, S. Ithurria, G. Vincent, B. Gallas, and E. Lhuillier, “Complex Optical Index of HgTe Nanocrystal Infrared Thin Films and Its Use for Short Wave Infrared Photodiode Design,” Adv. Opt. Mater. **9**, 2002066 (2021).
[24] A. Khalili, M. Weis, S.G. Mizrahi, A. Chu, T.H. Dang, C. Abadie, C. Gréboval, C. Dabard, Y. Prado, X.Z. Xu, E. Péronne, C. Livache, S. Ithurria, G. Patriarche, J. Ramade, G. Vincent, D. Boschetto, and E. Lhuillier, “Guided-Mode Resonator Coupled with Nanocrystal Intraband Absorption,” ACS Photonics **9**, 985 (2022).
[25] S. Keuleyan, E. Lhuillier, and P. Guyot-Sionnest, “Synthesis of Colloidal HgTe Quantum Dots for Narrow Mid-IR Emission and Detection,” J. Am. Chem. Soc. **133**, 16422 (2011).

[26] E. Lhuillier, M. Scarafagio, P. Hease, B. Nadal, H. Aubin, X.Z. Xu, N. Lequeux, G. Patriarche, S. Ithurria, and B. Dubertret, “Infrared Photodetection Based on Colloidal Quantum-Dot Films with High Mobility and Optical Absorption up to THz,” Nano Lett. **16**, 1282 (2016).
[27] S.-S. Chee, C. Gréboval, D.V. Magalhaes, J. Ramade, A. Chu, J. Qu, P. Rastogi, A. Khalili, T.H. Dang, C. Dabard, Y. Prado, G. Patriarche, J. Chaste, M. Rosticher, S. Bals, C. Delerue, and E. Lhuillier, “Correlating Structure and Detection Properties in HgTe Nanocrystal Films,” Nano Lett. **21**, 4145 (2021).
[28] B. Martinez, J. Ramade, C. Livache, N. Goubet, A. Chu, C. Gréboval, J. Qu, W.L. Watkins, L. Becerra, E. Dandeu, J.L. Fave, C. Méthivier, E. Lacaze, and E. Lhuillier, “HgTe Nanocrystal Inks for Extended Short-Wave Infrared Detection,” Adv. Opt. Mater. **7**, 1900348 (2019).
[29] X. Lan, M. Chen, M.H. Hudson, V. Kamysbayev, Y. Wang, P. Guyot-Sionnest, and D.V. Talapin, “Quantum dot solids showing state-resolved band-like transport,” Nat. Mater. **19**, 323 (2020).
[30] M.M. Ackerman, X. Tang, and P. Guyot-Sionnest, “Fast and Sensitive Colloidal Quantum Dot Mid-Wave Infrared Photodetectors,” ACS Nano **12**, 7264 (2018).
[31] S. Pierini, F. Capitani, M. Scimeca, S. Kozlov, D. Pierucci, R. Alchaar, C. Abadie, A. Khalili, M. Cavallo, T.H. Dang, H. Zhang, E. Bossavit, C. Gréboval, J. Avila, B. Baptiste, S. Klotz, A. Sahu, C. Feuillet-Palma, X.Z. Xu, A. Ouerghi, S. Ithurria, J.K. Utterback, S. Sauvage, and E. Lhuillier, “Vanishing Confinement Regime in Terahertz HgTe Nanocrystals Studied under Extreme Conditions of Temperature and Pressure,” J. Phys. Chem. Lett. **13**, 6919 (2022).
[32] N. Moghaddam, C. Gréboval, J. Qu, A. Chu, P. Rastogi, C. Livache, A. Khalili, X.Z. Xu, B. Baptiste, S. Klotz, G. Fishman, F. Capitani, S. Ithurria, S. Sauvage, and E. Lhuillier, “The Strong Confinement Regime in HgTe Two-Dimensional Nanoplatelets,” J. Phys. Chem. C **124**, 23460 (2020).
[33] E. Lhuillier, S. Keuleyan, and P. Guyot-Sionnest, “Optical properties of HgTe colloidal quantum dots,” Nanotechnology **23**, 175705 (2012).
[34] S. Godey, S. Dhellemmes, A. Wilk, M. Zaknoune, and F. Mollot, “CBr4 and Be heavily doped InGaAs grown in a production MBE system,” J. Cryst. Growth **278**, 600 (2005).
[35] Z. Deng, K.S. Jeong, and P. Guyot-Sionnest, “Colloidal Quantum Dots Intraband Photodetectors,” ACS Nano **8**, 11707 (2014).
[36] E. Lhuillier, M. Scarafagio, P. Hease, B. Nadal, H. Aubin, X.Z. Xu, N. Lequeux, G. Patriarche, S. Ithurria, and B. Dubertret, “Infrared Photodetection Based on Colloidal Quantum-Dot Films with High Mobility and Optical Absorption up to THz,” Nano Lett. **16**, 1282 (2016).
[37] C. Livache, B. Martinez, N. Goubet, C. Gréboval, J. Qu, A. Chu, S. Royer, S. Ithurria, M.G. Silly, B. Dubertret, and E. Lhuillier, “A colloidal quantum dot infrared photodetector and its use for intraband detection,” Nat. Commun. **10**, 2125 (2019).
[38] A. Khalili, M. Weis, S.G. Mizrahi, A. Chu, T.H. Dang, C. Abadie, C. Gréboval, C. Dabard, Y. Prado, X.Z. Xu, E. Péronne, C. Livache, S. Ithurria, G. Patriarche, J. Ramade, G. Vincent, D. Boschetto, and E. Lhuillier, “Guided-Mode Resonator Coupled with Nanocrystal Intraband Absorption,” ACS Photonics (2022).
[39] J. Qu, N. Goubet, C. Livache, B. Martinez, D. Amelot, C. Gréboval, A. Chu, J. Ramade, H. Cruguel, S. Ithurria, M.G. Silly, and E. Lhuillier, “Intraband Mid-Infrared Transitions in Ag2Se Nanocrystals: Potential and Limitations for Hg-Free Low-Cost Photodetection,” J. Phys. Chem. C **122**, 18161 (2018).
[40] S.B. Hafiz, M.R. Scimeca, P. Zhao, I.J. Paredes, A. Sahu, and D.-K. Ko, “Silver Selenide Colloidal Quantum Dots for Mid-Wavelength Infrared Photodetection,” ACS Appl. Nano Mater. **2**, 1631 (2019).
[41] S.B. Hafiz, M.M. Al Mahfuz, and D.-K. Ko, “Vertically Stacked Intraband Quantum Dot Devices for Mid-Wavelength Infrared Photodetection,” ACS Appl. Mater. Interfaces **13**, 937 (2021).
[42] S.B. Hafiz, M.M. Al Mahfuz, S. Lee, and D.-K. Ko, “Midwavelength Infrared p–n Heterojunction Diodes Based on Intraband Colloidal Quantum Dots,” ACS Appl. Mater. Interfaces **13**, 49043 (2021).